



Contents lists available at ScienceDirect

## Arabian Journal of Chemistry

journal homepage: [www.ksu.edu.sa](http://www.ksu.edu.sa)

Original article

## Phosphate removal performance and mechanism of zirconium-doped magnetic gasification slag

Baoguo Yang<sup>a,b</sup>, Fengcheng Jiang<sup>c,\*</sup>, Yinxin Zhao<sup>d,\*</sup>, Hongbin Li<sup>a</sup>, Shengguang Zhang<sup>a</sup>, Kanghui Liu<sup>a</sup><sup>a</sup> School of Resources and Environment, Yili Normal University, Yining 835000, China<sup>b</sup> Xinjiang Key Laboratory of Clean Conversion and High Value Utilization of Biomass Resources, Yili Normal University, Yining 835000, China<sup>c</sup> School of Resources and Environment, Henan Polytechnic University, Jiaozuo 454003, China<sup>d</sup> Ningxia Hui Autonomous Region Basic Geological Survey Institute, Yinchuan 750000, China

## ARTICLE INFO

## Keywords:

Phosphorous  
Zr  
Solid waste  
Adsorption  
Wastewater

## ABSTRACT

Zirconium-modified materials exhibit good adsorption performance, but their large-scale application is limited by the cost of carrier materials and the difficulty of solid-liquid separation of powder adsorbents. Therefore, in this study, we used low-cost gasification slag for zirconium oxide loading to avoid the aforementioned problems and successfully prepared a novel gasification slag-based zirconium-doped magnetic adsorbent material (GS-Z2M). GS-Z2M is a mesoporous adsorbent material with a large specific surface area (188 m<sup>2</sup>/g); it completely adsorbed phosphate with an initial concentration of 10 mg/L within 3 h. The rate-controlling step of phosphate removal using GS-Z2M was chemisorption. The Langmuir model proved more suitable for describing the adsorption of phosphate on GS-Z2M than the Freundlich and Temkin models, and the maximum phosphate adsorption capacity calculated using the Langmuir model was 26.02 mg/g. GS-Z2M showed good phosphate adsorption selectivity and reusability (can be recycled at least 5 times). GS-Z2M also showed good capacity for treating actual phosphate wastewater under dynamic flow conditions. The mechanism of phosphate adsorption on GS-Z2M mainly involved ligand exchange and inner-sphere complexation. The obtained results suggest that GS-Z2M is a promising adsorbent and vital for the development of phosphate adsorbents and recycling of gasification slag.

## 1. Introduction

Phosphate, a key nutrient for aquatic plant growth, can promote algal blooms, reduce water quality and affect the ecological health of aquatic ecosystems when present in excessive amounts (Huo et al., 2021). With the widespread use of phosphorus-containing substances, phosphate pollution in water has become a serious environmental problem, leading to the eutrophication of water bodies and subsequent ecological imbalances (Yang et al., 2023a). Therefore, efficient and cost-effective methods for phosphate removal from wastewater are urgently needed.

Various approaches have been developed for the removal of phosphate from wastewater, including chemical precipitation, biological treatment, ion exchange and adsorption (Yang et al., 2023b). Chemical precipitation requires large quantities of chemicals, leading to high treatment costs and risks of secondary environmental pollution.

Meanwhile, biological treatments involve long processing cycles and require specific wastewater conditions. Ion exchange treatments, while effective, are costly, demand stringent operating conditions and offer limited selectivity. Among these methods, adsorption is considered promising because of its simplicity, high efficiency and ease operation (Bacelo et al., 2020). However, the success of adsorption techniques largely depends on the selection of suitable adsorbents, which should have high adsorption capacity, good selectivity, good stability and low cost. Some researchers have explored metal-modified adsorbent materials for phosphate removal, including lanthanum-carbonate-modified zeolite-derived materials (Yang et al., 2022c), lanthanum carbonate loaded microfiber composite materials (Yang et al., 2020), iron-lanthanum bimetallic carbon nanotube films (Yang et al., 2024b), lanthanum-carbonate-loaded microfiber composites (Yang et al., 2024a), Zr-based metal-organic frameworks with Fe and Ce bimetal for magnetic adsorption (Yang et al., 2022b), polyethylene imine and

\* Corresponding authors.

E-mail addresses: [fc.jiang@hpu.edu.cn](mailto:fc.jiang@hpu.edu.cn) (F. Jiang), [zhaoYX04@163.com](mailto:zhaoYX04@163.com) (Y. Zhao).<https://doi.org/10.1016/j.arabjc.2024.106079>

Received 6 August 2024; Accepted 5 December 2024

Available online 10 December 2024

1878-5352/© 2024 The Author(s). Published by Elsevier B.V. on behalf of King Saud University. This is an open access article under the CC BY-NC-ND license (<http://creativecommons.org/licenses/by-nc-nd/4.0/>).

carboxymethyl cellulose composites (Yang et al., 2021) and metal-organic frameworks (Peng et al., 2024). However, these adsorbent materials encounter limitations, including limited availability, complex preparation processes and poor stability in acidic environments.

Given the adsorption affinity of Zr for phosphate and the good stability of Zr-modified materials in acidic environments (Sun et al., 2018), researchers have recently focused on using these materials for phosphate adsorption. Currently, most Zr-modified materials include synthetic zeolite (Xie et al., 2017), biochar (Aryee et al., 2021) and minerals (Huo et al., 2021). However, these carrier materials also present drawbacks, such as limited availability, high energy consumption and considerable preparation costs, underscoring the need to identify widely available and cost-effective alternatives.

In recent years, adsorbents derived from industrial waste materials have attracted considerable attention. Such adsorbents not only offer economic advantages but also contribute to waste reduction and recycling. A previous study compared and analysed the phosphate removal performance of blast furnace sludge and Kanbara reactor powder from water. The two waste materials achieved a phosphate removal efficiency of ~99 % within 24 h. In addition, regardless of the solution pH, a phosphate removal rate of ~97 % was achieved within the first 10 min of adsorption (Da Silva et al., 2022). Fly ash–biochar–iron and coal gangue–biochar–iron have been prepared by mixing fly ash and coal gangue with pine wood, followed by carbonisation, activation and impregnation with ferric chloride; these materials showed phosphate adsorption capacities of 3.08 and 3.2 mg/g, respectively (Qiu and Duan, 2019). Copper nitrate solutions with different initial concentrations have also been used to modify X-type zeolite derived from fly ash, resulting in a maximum adsorption capacity of 87.7 mg/g (Mokrzycki et al., 2022). These studies have shown that the phosphate adsorption performance of different solid waste materials varies and the phosphate adsorption capacity of most pure solid waste materials is limited. However, as of now, few studies have focused on the removal of phosphate from water using coal gasification slag (CGS), which is a by-product of coal gasification (Miao et al., 2022). The rapid development of coal gasification technology has led to a significant increase in CGS emissions, and the treatment of CGS has gradually attracted considerable attention (Guo et al., 2023). China has been reported to produce over 70 million tonnes of CGS annually, with only a very small portion of it utilised and a major portion simply dumped or landfilled (Zhu et al., 2024). The dumping or landfilling of a large amount of CGS causes waste of land resources and poses a potential threat to the surrounding environment (Su et al., 2024). Coal gasification coarse slag (CGCS) is a type of CGS with well-developed pores and a certain specific surface area (10 m<sup>2</sup>/g) (Shu et al., 2022; Yang et al., 2023c). Compared to mineral materials and other carriers, such as zeolite, biochar and clay minerals, CGCS offers advantages in terms of large reserves, easy availability and low cost. Therefore, it is necessary and important to study phosphate adsorption using CGCS-based adsorbents.

Our research team has conducted early-stage studies on phosphate removal using CGCS (Yang et al., 2022a; Yang et al., 2023c) and found that CGCS has excellent phosphate adsorption performance, but encounters difficulties in solid–liquid separation. Therefore, we integrated magnetic properties into the adsorbent in this study for easy separation and recycling. To further enhance the phosphate adsorption performance of magnetic CGCS, zirconia was introduced into it. The individual phosphate adsorption capacities of pure zirconia (HZO), Fe<sub>3</sub>O<sub>4</sub> and CGCS are limited. However, combining these three materials can considerably enhance phosphate adsorption, improving the adsorption performance of CGCS while also addressing challenges of solid–liquid separation. In this study, the use of CGCS enabled effective phosphate removal from water, exemplifying an innovative approach of using waste materials to treat pollutants.

In this study, we focused on 1) synthesising a novel Zr-doped magnetic CGCS adsorbent for phosphate removal and characterising related materials, 2) exploring the phosphate removal performance of the

adsorbent under external conditions (such as in the presence of competing ions and at different pH levels) and 3) determining possible phosphate removal mechanisms. This article proposes a new approach for the preparation of phosphate removal adsorbents for wastewater remediation and CGCS utilisation.

## 2. Materials and methods

### 2.1. Materials

CGCS was obtained from a chemical enterprise in Ningxia; it was ground and sieved through a 200-mesh sieve. It consisted of SiO<sub>2</sub> (55.5 %), Al<sub>2</sub>O<sub>3</sub> (15.6 %), CaO (10.9 %), Fe<sub>2</sub>O<sub>3</sub> (8.1 %), MgO (2.26 %), C (2.9 %), Na<sub>2</sub>O (1.52 %), K<sub>2</sub>O (1.23 %), TiO<sub>2</sub> (0.72 %) and other compounds (1.27 %).

Ferrous sulphate heptahydrate (FeSO<sub>4</sub>·7H<sub>2</sub>O), ferric chloride hexahydrate (FeCl<sub>3</sub>·6H<sub>2</sub>O), sodium hydroxide (NaOH) and hydrochloric acid (HCl) were purchased from Sinopharm Group, and potassium dihydrogen phosphate (KH<sub>2</sub>PO<sub>4</sub>) and potassium antimony tartrate (C<sub>4</sub>H<sub>4</sub>KO<sub>7</sub>Sb<sup>-1</sup>/2H<sub>2</sub>O) were purchased from Tianjin Kemiou, China. Synthetic wastewater with different phosphate concentrations was prepared by diluting a 1000 mg/L stock solution of KH<sub>2</sub>PO<sub>4</sub>. All reagents were AR-grade.

### 2.2. Preparation of materials

The magnetic adsorption materials were prepared from CGCS via a one-step co-precipitation method (Fig. S1). Specifically, 1.61 g of CGCS, FeSO<sub>4</sub>·7H<sub>2</sub>O and FeCl<sub>3</sub>·6H<sub>2</sub>O were weighed and added to a 250-mL conical flask at Zr:Fe<sub>3</sub>O<sub>4</sub> molar ratios of 1:2, 1:1, 2:1 and 3:1. Then, 50 mL of deionised (DI) water was added, and the mixture was magnetically stirred, ultrasonicated for 2 min and further stirred for 20 h. The mixture was subsequently heated to 60 °C, and NaOH was added dropwise until the pH of the mixture reached 12. The mixture was then further heated and stirred for a certain period, followed by washing with deionised water until neutral pH level was attained and then dried at 70 °C in a blast drying oven, yielding the target adsorbent materials. The materials with Zr:Fe<sub>3</sub>O<sub>4</sub> molar ratios of 1:2, 1:1, 2:1 and 3:1 were named CS-ZM2, CS-ZM, CS-Z2M and CS-Z3M, respectively. The preparation of HZO and Fe<sub>3</sub>O<sub>4</sub> was performed under similar conditions as mentioned above, except for the absence of CGCS.

### 2.3. Sample characterizations

The chemical composition of CGCS and CS-Z2M were determined via X-ray fluorescence spectroscopy (Panalytical Axios, Netherlands). Microstructure and surface elemental composition were determined via scanning electron microscopy and energy-dispersive spectroscopy (SEM-EDS); Zeiss Gemini 300, Germany). Functional groups were detected using Fourier transform infrared (FTIR) spectroscopy (Thermo Scientific Nicolet 6700, USA). Crystalline properties were evaluated through X-ray diffraction (XRD; LabX XRD-6000, Japan) with Cu K $\alpha$  radiation (40 kV, 30 mA) at a rate of 2°/min over a scanning range of 10–80°. Elemental composition and binding energies were analysed using X-ray photoelectron spectroscopy (Thermo Scientific K-Alpha, USA). The point of zero charge (pH<sub>PZC</sub>) of the samples was evaluated using the pH drift method (Zhao et al., 2020).

### 2.4. Adsorption experiments

The adsorbents were added to 50 mL of a phosphate solution with a certain concentration and an initial pH of 6 at a dosage of 1 g/L and allowed to react in a water bath shaker at 25 °C for 24 h. After the reaction, the mixtures were centrifuged, and the residual phosphate concentration in the supernatants was determined using molybdenum antimony spectrophotometry. The method used to determine the

adsorption capacity ( $q$ ) is described in detail in Text S1 (Supplementary Materials).

The initial pH of the solution was adjusted to 3–10 using 0.1 M HCl or NaOH to evaluate the effect of pH levels on the phosphate adsorption performance of the adsorbents. The effects of different anions and humic acid (HA) on the phosphate removal performance of the prepared adsorbents were studied using NaCl, Na<sub>2</sub>SO<sub>4</sub>, NaNO<sub>3</sub> and NaHCO<sub>3</sub> solutions with concentrations of 1 and 10 mM as well as HA solutions with concentrations of 35 and 70 mg/L. Adsorption isotherms were obtained in a phosphate concentration range of 20–65 mg/L. Finally, adsorption kinetics were investigated in the duration range of 0.5–11 h. All the adsorption experiments were conducted thrice.

Saturated magnetic adsorbents were desorbed for 24 h in a constant-temperature water bath shaker at 160 rpm using 50 mL of a 1 mol/L NaOH solution. Then, the adsorbents were washed several times with DI water and dried. After desorption, they were used in the next phosphate adsorption experiment. Thus, five adsorption–desorption cycles were performed to evaluate the desorption and regeneration performance of the adsorbents.

Further, leaching tests were performed to investigate the metal leaching of GS-Z2M in DI water and phosphate solutions. For the tests, 50 mg of GS-Z2M was added separately to 250-mL conical flasks containing 50 mL of DI water and a phosphate solution (40 mg/L). These solutions were then agitated at 160 rpm for 24 h in a water bath oscillator at pH = 3 and 6. The toxicity leaching tests were conducted using the horizontal vibration method (HJ 557-2010). In this study, reaction time and rotational speed were based on preliminary experiments. We compared adsorption effects at 12, 24 and 48 h, finding that adsorption equilibrium was nearly realised at 24 h. Similarly, we evaluated adsorption effects at rotational speeds of 120, 160 and 200 rpm, selecting 160 rpm to achieve optimal balance between energy efficiency and adsorption performance.

Dynamic flow tests were also conducted with synthetic and actual wastewater samples to evaluate the phosphate removal performance of GS-Z2M under dynamic flow conditions. These experiments were conducted in a Plexiglas tube with an inner diameter of 12 mm and a length of 130 mm. In particular, 2.5 g of GS-Z2M (~3-cm bed height) was placed at the centre of the tube and balls of skimmed cotton wool were placed at the top and bottom of the tube to prevent sample loss. A peristaltic pump (Rongbai BT 100) controlled the flow rate at 1 mL/min (Yang et al., 2023c; Yin et al., 2017). Wastewater entered from the bottom of the tube and exited from the top, where treated water was collected and analysed for determining residual phosphate concentration.

### 3. Results and discussion

#### 3.1. Phosphate adsorption

##### 3.1.1. Effects of the Zr/magnetite molar ratios on the phosphate adsorption capacity

As illustrated in Fig. 1, the individual phosphate adsorption capacities of HZO, Fe<sub>3</sub>O<sub>4</sub> and CGCS are limited. However, combining these three materials results in improved adsorption capacity, likely attributed to their synergistic effect, as confirmed by FTIR analysis. Preliminary experiments demonstrated that the simultaneous deposition of Zr and Fe resulted in faster magnetic separation properties of the prepared adsorbents than when Zr was loaded onto magnetic CGCS after Fe (Fig. S2). Therefore, based on the results of the preliminary experiments, magnetic adsorbents for the main experiments were prepared through the simultaneous precipitation of Zr and Fe. As the Zr content increased, the phosphate adsorption capacity of the obtained adsorbents increased. GS-Z2M exhibited the best adsorption capacity among the prepared adsorbents, which was attributed to the good adsorption affinity of Zr towards phosphate. However, a high Zr content does not necessarily result in better adsorption capacity. Above a certain value, an increase in the

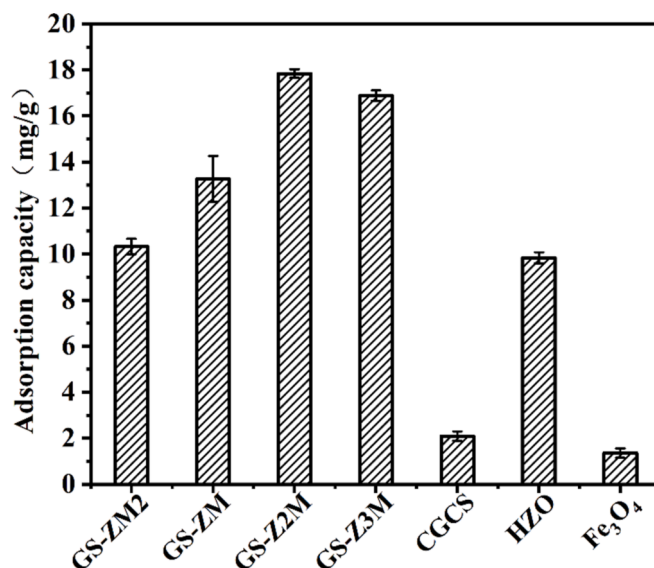


Fig. 1. Effects of zirconium/magnetite mole ratio on phosphate adsorption capacity. Adsorption conditions: temperature: 25 °C; oscillation rate: 160 rpm; reaction time: 24 h; sorbent dose: 1 g/L; pH: 6; phosphate concentration: 40 mg/L.

Zr content causes a decrease in the adsorption capacity. This may be attributed to the aggregation of nano-zirconium oxide, resulting in a decrease in the specific surface area. Nanoparticles exhibit exceptionally large specific surface areas owing to their small sizes, which results in strong van der Waals forces and other surface interactions between them, making them susceptible to agglomeration. Therefore, GS-Z2M was selected as the optimal adsorbent for subsequent experiments.

##### 3.1.2. Influence of solution pH on the phosphate adsorption capacity

Phosphate species in the reaction solution and surface charge properties of GS-Z2M were both affected by solution pH; therefore, the elucidation of the effect of pH levels on the on adsorption performance was particularly important. The phosphate adsorption capacity of GS-Z2M decreased with increasing pH (Fig. 2). The adsorption of phosphate on GS-Z2M was significantly affected by the solution pH. Under acidic conditions, GS-Z2M exhibited a high phosphate adsorption capacity. With increasing pH, the adsorption capacity gradually decreased,

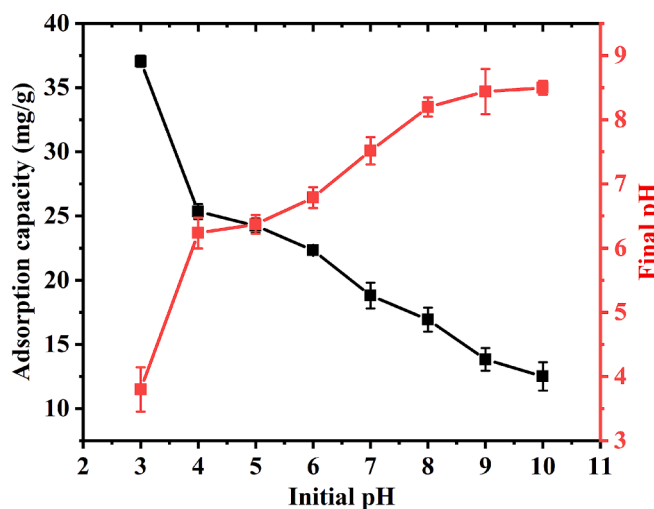


Fig. 2. Variation of phosphate adsorption capacity of GS-Z2M with respect to pH. Adsorption conditions: temperature: 25 °C; oscillation rate: 160 rpm; reaction time: 24 h; sorbent dose: 1 g/L; phosphate concentration: 60 mg/L.

indicating that acidic conditions are more conducive to phosphate adsorption. As detailed in Text S2 (Supplementary Materials), within the pH range of 3–10, phosphate mainly exists in the form of  $\text{H}_2\text{PO}_4^-$  and  $\text{HPO}_4^{2-}$  (Abdellaoui et al., 2021; Xiong et al., 2017). The  $\text{pH}_{\text{PZC}}$  of GS-Z2M was found to be 8.2 (Fig. 10). At pH values of  $<8.2$ , the surface of GS-Z2M was positively charged, resulting in the electrostatic adsorption of  $\text{H}_2\text{PO}_4^-$  and  $\text{HPO}_4^{2-}$  (Asaoka et al., 2021; Yu et al., 2015). At pH values of  $>8.2$ , the surface of GS-Z2M became negatively charged, leading to the repulsion between the adsorbent and negatively charged  $\text{H}_2\text{PO}_4^-$  and  $\text{HPO}_4^{2-}$ , reducing the adsorption performance. At the same time, with increasing pH, the concentration of  $\text{OH}^-$  increased, resulting in a competition for adsorption sites between the phosphate ions and  $\text{OH}^-$  (Yang et al., 2024a).

Notably, the final pH of the reaction solution increased when initial pH was 3–9. This was attributed to ligand exchange between phosphate ions and the hydroxyl groups on the surface of GS-Z2M, which increased the concentration of  $\text{OH}^-$  in the reaction solution, leading to an increase in the pH level (Liao et al., 2018). For initial pH values of  $>9$ , the final pH decreased, which was attributed to the higher adsorption of  $\text{OH}^-$  on GS-Z2M compared to phosphate ions in a strongly alkaline environment, resulting in a decrease in the concentration of  $\text{OH}^-$  in the reaction solution (Araújo et al., 2018; Yang et al., 2024a).

### 3.1.3. Effects of coexisting anions and HA

In practical application, organic matter and coexisting anions (such as HA, nitrate, sulphate and bicarbonate) in water bodies may affect the phosphate removal performance of adsorbents. Therefore, the phosphate removal performance of GS-Z2M in the presence of competing ions was investigated. As shown in Fig. 3, competitive anions did not significantly affect phosphate removal by GS-Z2M. According to a previous study (Min et al., 2019), outer-sphere complexation is affected by the concentration of competitive anions while inner-sphere complexation is insensitive to it. Therefore, the binding of phosphate to GS-Z2M likely occurred through inner-sphere complexation. Similar phenomena have also been reported in other studies (Liu et al., 2019a; Liu et al., 2019b).

The results of competitive adsorption experiments indicated that GS-Z2M selectively adsorbed phosphate; the adsorbent could later be leveraged to recover high-purity phosphate through desorption and regeneration. Thus, GS-Z2M is a promising phosphate adsorbent. HA, a macromolecular natural organic matter widely present in nature, contains active functional groups (such as carboxyl, phenolic and ketone

groups) that usually affect the performance of adsorbents. Herein, HA affected the removal of phosphate by GS-Z2M, but to a limited extent. With increasing concentration of HA, its adsorption also increased. Given the complex structure of HA, the mechanism of this effect needs to be further studied.

### 3.1.4. Adsorption isotherms

To evaluate the adsorption capacity of GS-Z2M, its adsorption isotherm was obtained. As shown in Fig. 4 and Table S1, the maximum phosphate adsorption capacity of GS-Z2M was 26.02 mg/g, exceeding the adsorption capacities of most previously reported zirconium-, lanthanum- and solid-waste-based adsorbents (Table S2).

To explore the possible mechanism of the reaction between GS-Z2M and phosphate, the experimental adsorption data were fitted and analysed using Langmuir, Freundlich and Temkin models (Text S3). As detailed in Table S1, the Langmuir model showed a higher fitting coefficient ( $R^2 = 0.992$ ) compared to greater than those of the Freundlich ( $R^2 = 0.965$ ) and Temkin models ( $R^2 = 0.958$ ), indicating that phosphate adsorption onto GS-Z2M likely occurred through monolayer adsorption (Huang et al., 2020; Xiong et al., 2017), and the GS-Z2M surface was likely homogeneous (Koh et al., 2020). The Langmuir isotherm model assumes a homogeneous adsorbent surface with independent adsorption sites, where no spatial hindrance exists between adjacent sites, resulting in single-layer adsorption. In contrast, the Freundlich model applies to multi-layer adsorption on heterogeneous surfaces, while the Temkin model assumes that the adsorption heat of all molecules within the adsorption layer decreases linearly with increasing surface coverage (Araújo et al., 2018; Kegl et al., 2020; Li et al., 2020; Usman and Khan, 2022).

### 3.1.5. Adsorption kinetics

Adsorption kinetics are important for evaluating adsorbents. Phosphate adsorption kinetics on GS-Z2M are shown in Fig. 5 and Table S3. At an initial concentration of 10 mg/L, phosphate was almost completely adsorbed within 3 h (Fig. 5a), indicating that GS-Z2M can rapidly remove phosphate.

To further explore the adsorption mechanism, two commonly used kinetic models (Text S4) were employed to fit the experimental data (Table S3). The pseudo-second-order equation suggests that the adsorption rate is proportional to the number of active adsorption sites, indicating that the process is reversible. This model also implies that the

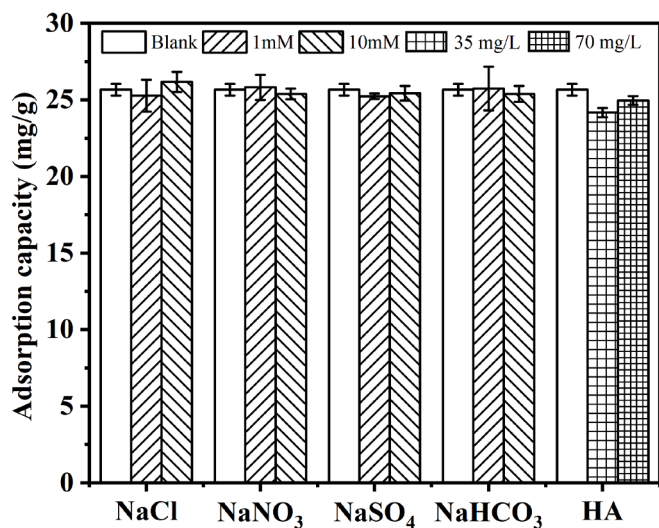


Fig. 3. Effects of coexistent anions and humic acid. Adsorption conditions: temperature: 25 °C; reaction time: 24 h; sorbent dose: 1.0 g/L; phosphate concentration: 40 mg/L.

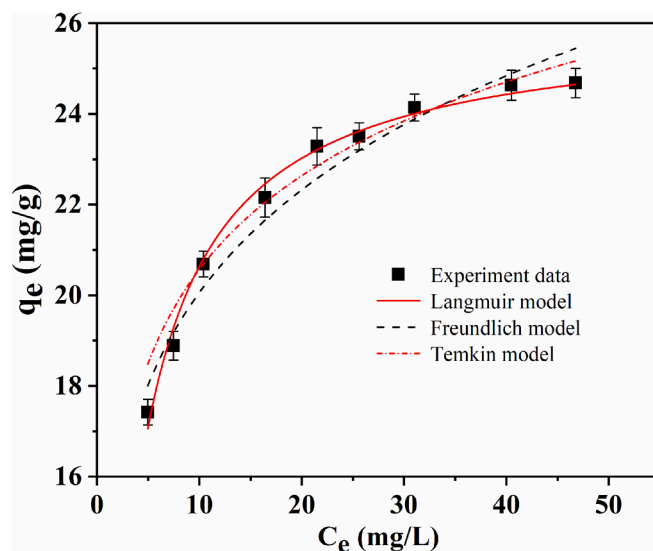


Fig. 4. Langmuir, Freundlich and Temkin adsorption isotherm of GS-Z2M. Adsorption conditions: oscillation time, 24 h; sorbent dose, 1.0 g/L; temperature, 25 °C; initial phosphate concentration, 20–65 mg/L.

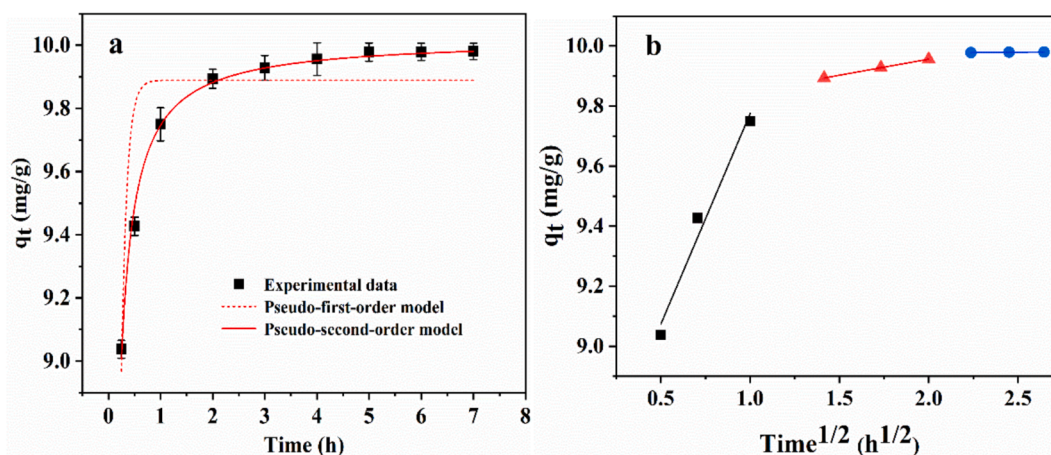


Fig. 5. Adsorption kinetics plots fitted with (a) pseudo-first-order, pseudo-second-order model, and (b) intraparticle diffusion models. Adsorption conditions: temperature, 25 °C; adsorbent dose, 1.0 g/L; initial phosphate concentration, 10 mg/L.

rate-controlling step most likely involves chemical interactions, primarily indicating that the adsorption process between the adsorbent and adsorbate is chemical adsorption (Guo et al., 2021). The results indicate that the  $R^2$  value for the pseudo-second-order equation (0.993) was higher than that for the pseudo-first-order equation (0.786), with the fitted values ( $q_{e,cal} = 10.02$ ) obtained using the pseudo-second-order equation being very close to the experimental data ( $q_{e,exp} = 9.99$ ). Therefore, the pseudo-second-order equation better described the phosphate removal process of GS-Z2M. Thus, the rate-controlling step of phosphate removal by GS-Z2M was chemical adsorption (Jung et al., 2019).

To further clarify the diffusion mechanism and rate-limiting step, the experimental data were simulated using the intraparticle diffusion model. As depicted in Fig. 5b, the fitting curve comprises three straight lines, each representing a stage in the adsorption of phosphate onto GS-Z2M. The first stage reflects the rapid migration of phosphate ions from the bulk solution to the surface of GS-Z2M, primarily controlled by membrane or boundary layer diffusion. In the second stage, phosphate ions transfer from the external surface of GS-Z2M to internal adsorption sites, with the rate-limiting step being intra-particle or pore diffusion. The third stage signifies adsorption equilibrium, where the adsorption rate decreases substantially until stabilisation, indicating that the adsorption sites are fully occupied. The second segment does not pass through the origin ( $C \neq 0$ ; Table S3), suggesting that the adsorption rate is controlled by multiple stages. The slope of the first stage exceeds that of the second stage ( $k_{id1} > k_{id2}$ ; Table S3), suggesting that membrane diffusion or boundary layer transport is the main rate-controlling step, intra-particle diffusion in the second stage is a secondary rate-limiting step and the third stage corresponds to the attainment of adsorption equilibrium (Jung et al., 2019; Konicki et al., 2017; Shan et al., 2019).

### 3.1.6. Reusability of the adsorbents

Cyclic adsorption performance is one of the important indicators of comprehensive adsorbent performance; thus, the reusability of GS-Z2M was explored. As shown in Fig. 6, the adsorption capacity decreases with cycling, attributed to the formation of inner-sphere complexes between phosphate ions and GS-Z2M, which are more difficult to desorb than physically adsorbed phosphate ions (Huang et al., 2020). In addition, according to the results of the metal ion leaching experiments discussed in Section 3.1.7, a small amount of Fe ions leached from GS-Z2M in water, and the number of effective active sites on GS-Z2M gradually decreased with cycling, resulting in a corresponding decrease in the adsorption capacity. Nevertheless, the phosphate adsorption capacity of GS-Z2M in the fifth cycle remained above 57 % that in the first cycle, indicating that GS-Z2M has good reusability and is a promising phosphate adsorbent.

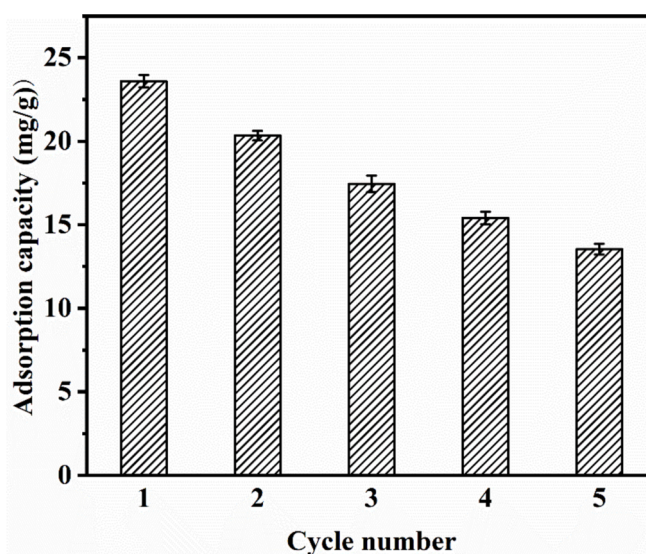


Fig. 6. Relationship between the adsorption capacity of GS-Z2M and the number of cycles. Adsorption conditions: GS-Z2M dose: 1.0 g/L; initial phosphate concentration: 40 mg/L; eluant: 50 mL of 1 M NaOH; reaction time: 24 h; temperature: 25 °C.

### 3.1.7. Metal leaching

To investigate whether GS-Z2M causes secondary environmental pollution during phosphate removal, we conducted heavy-metal leaching experiments and analysed the leaching of Zr and Fe in DI water and phosphate solutions. As shown in Table S4, the content of heavy metals leached from GS-Z2M is lower than the concentration limit of Class I surface water prescribed in China's surface water environmental quality standards (GB 3838-2002). This proves that GS-Z2M is safe and does not cause secondary pollution. The analysis results of Zr and Fe leaching in DI water and residual phosphate solution after phosphate adsorption (Table S5) indicate that a small amount of Fe and Zr was leached in DI water. However, the leaching amount is negligible, indicating that GS-Z2M can be considered inert and safe (Dou et al., 2011; Khan and Sharma, 2019). Interestingly, the Fe content in the residual phosphate solution after phosphate removal was significantly lower than that in DI water, indicating the occurrence of reactions between Fe and phosphate.

### 3.1.8. Column adsorption tests

To evaluate the performance of GS-Z2M in treating real phosphate wastewater under dynamic flow conditions, fixed-bed experiments were

conducted. The breakthrough point in these experiments was set at 0.5 mg/L, based on the phosphate concentration limit specified in the Chinese urban wastewater control standard (GB 18918-2002). The experimental phosphate wastewater was collected from the secondary sedimentation tank of a wastewater treatment plant in Yinchuan, and its primary components are listed in Table S6. For the comparison of the experimental wastewater with synthetic wastewater, the initial phosphate concentration was adjusted to 5 mg/L. The dynamic column had an empty bed volume (BV) of 3.39 mL with a flow rate of 1 mL/min. As illustrated in Fig. 7, GS-Z2M demonstrated good performance in treating actual phosphate wastewater under dynamic flow conditions, processing over 199 BV of the real wastewater. Meanwhile, GS-Z2M treated more than 294 BV of the synthetic wastewater. This discrepancy is likely attributed to the presence of impurity ions in the actual wastewater, interfering with phosphate adsorption.

### 3.2. Phosphate removal mechanism

#### 3.2.1. Morphological and structural characterisation of the adsorbents

The morphologies and elemental compositions of CGCS, GS-Z2M and GS-Z2M after phosphate adsorption are illustrated in Fig. 8. The morphology of CGCS comprises irregular blocks of different sizes. After the introduction of Fe and Zr, CGCS transformed into GS-Z2M, showing flocculent and regular crystalline substances. EDS results showed Zr and a large amount of Fe in GS-Z2M, indicating that zirconium and iron were successfully loaded onto CGCS. XRD results suggested that these flocculent substances may be zirconium oxides while the regular crystalline substances are magnetic Fe<sub>3</sub>O<sub>4</sub>. After phosphate adsorption onto GS-Z2M, numerous tiny particles were observed on the surfaces of the flocculent and regular crystalline structures. EDS analysis revealed new phosphorus signals, indicating successful phosphorus adsorption onto GS-Z2M.

The specific surface area and pore size of GS-Z2M and CGCS were studied using N<sub>2</sub> adsorption-desorption isotherms and Barrett-Joyner-Halenda pore size distribution, respectively (Fig. 9 and Table S7). According to IUPAC definitions (Thommes et al., 2015), both GS-Z2M and CGCS exhibited type IV isotherms and H3 hysteresis loops (Fig. 9a), suggesting the presence of slit-shaped pores (Zhou et al., 2011; Zhu et al., 2021). The hysteresis loop observed at P/P<sub>0</sub> > 0.8 further indicated that GS-Z2M predominantly comprised mesoporous structures (Wang et al., 2015). The pore size distributions of GS-Z2M and CGCS (Fig. 9b) confirmed their mesoporous nature, with pore sizes mainly

concentrated in the range of 3–4 nm. The specific surface area of GS-Z2M was 188 m<sup>2</sup>/g, nearly 19 times that of CGCS (Table S7), while its cumulative pore volume was 0.2097 cm<sup>3</sup>/g, more than 16 times that of CGCS. Such mesoporous structures and large specific surface areas greatly enhanced the phosphate adsorption performance of the adsorbent.

#### 3.2.2. pH<sub>PZC</sub>

The change in the pH<sub>PZC</sub> value after adsorption can help elucidate the adsorption reaction mechanism of phosphate, as shown in Fig. 10. The initial pH<sub>PZC</sub> of GS-Z2M was 8.2. After phosphate adsorption, the pH<sub>PZC</sub> value decreased to 6.3, indicating specific adsorption and formation of inner-sphere complexes. Generally, the formation of outer-sphere complexes does not alter the isoelectric point of an adsorbent because of insufficient interaction between the adsorbent and adsorbate (Huo et al., 2021). In contrast, inner-sphere complexes (specific adsorption) of anions increase the negative charge of the adsorbent surface, resulting in a shift in the pH<sub>PZC</sub> value of the adsorbent towards a lower isoelectric point (He et al., 2017).

#### 3.2.3. XRD results

As illustrated in Fig. 11, the main crystal phase of CGCS was SiO<sub>2</sub>. After the introduction of Zr and Fe into CGCS, Fe<sub>3</sub>O<sub>4</sub> was detected, indicating that magnetite was successfully loaded onto CGCS. Further, no crystal phases of Zr were detected, indicating that Zr was present in an amorphous form in GS-Z2M. The intensity of quartz peaks significantly decreased after the introduction of Zr and Fe, and some quartz peaks disappeared, indicating that sodium hydroxide and quartz underwent a chemical reaction during modification, damaging the crystal structure of quartz. After the adsorption of phosphate on GS-Z2M, no significant changes were observed in the crystalline state of GS-Z2M, indicating that phosphate mainly existed in an amorphous form.

#### 3.2.4. FTIR results

As illustrated in Fig. 12, the bands at 3423 and 1627 cm<sup>-1</sup>, assigned to the vibrations and deformation of constitutive water (O–H) (De Filippis et al., 2021; Varas et al., 2005), were observed in the spectra of all samples. The band at 1058 cm<sup>-1</sup> was a characteristic of Si–O stretching vibrations in silica or silicates (Navarro et al., 2010; Yuan et al., 2022), and the band at 481 cm<sup>-1</sup> was assigned to Si–O–Si or Si–O–Al symmetric stretching or bending vibration (Wu et al., 2021; Yang et al., 2023b). After modification with Zr and Fe (GS-Z2M), the intensity of these characteristic peaks decreased and the peak positions shifted, indicating that zirconia and magnetite were generated along with the decomposition of the original quartz or silicate components by alkaline solutions, consistent with the XRD results. The peaks around 571 and 556 cm<sup>-1</sup> were attributed to the stretching vibrations of the Fe–O bonds in Fe<sub>3</sub>O<sub>4</sub> (Alamgholiloo et al., 2021; Xu et al., 2022). The positions of the Fe–O peaks of Fe<sub>3</sub>O<sub>4</sub> in GS-Z2M shifted after phosphate adsorption, indicating that Fe<sub>3</sub>O<sub>4</sub> not only participated in phosphate adsorption but also maintained magnetism after phosphate adsorption, which is beneficial for solid-liquid separation. The peak at 945 cm<sup>-1</sup> corresponded to hydroxyl group deformation (Navarro et al., 2010), and the peaks at 1575 and 1361 cm<sup>-1</sup> corresponded to Zr–OH vibrations (Yang et al., 2022a); these peaks disappeared after the adsorption of phosphate on GS-Z2M, indicating that hydroxyl groups and Zr–OH on GS-Z2M underwent ligand exchange with phosphate, forming inner-sphere complexes. The peaks around 973 and 556 cm<sup>-1</sup> were attributed to the stretching vibrations of P–O bonds in the phosphate group (Coulibaly et al., 2016; Kumar et al., 2021). The emergence of these P–O peaks confirmed that phosphate adsorption was dominated by chemisorption and formation of inner-sphere complexes, consistent with the results presented in Section 3.3.1.

In summary, by analyzing the effect of solution pH on phosphate adsorption, changes in pH<sub>PZC</sub> before and after phosphate adsorption, FTIR analysis, etc., the mechanism of phosphate adsorption on GS-Z2M

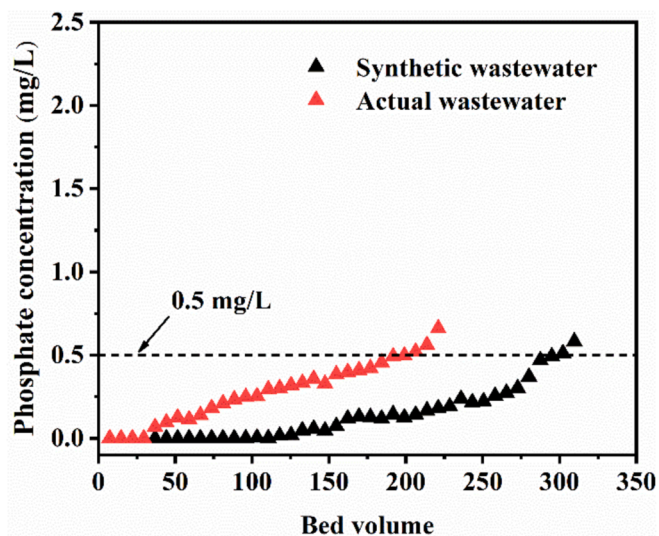


Fig. 7. Dynamic column penetration curves of GS-Z2M treated synthetic wastewater versus actual wastewater. Adsorption conditions: influent phosphate concentration, 5 mg/L; flow rate, 1 mL/min; temperature, 25 °C.

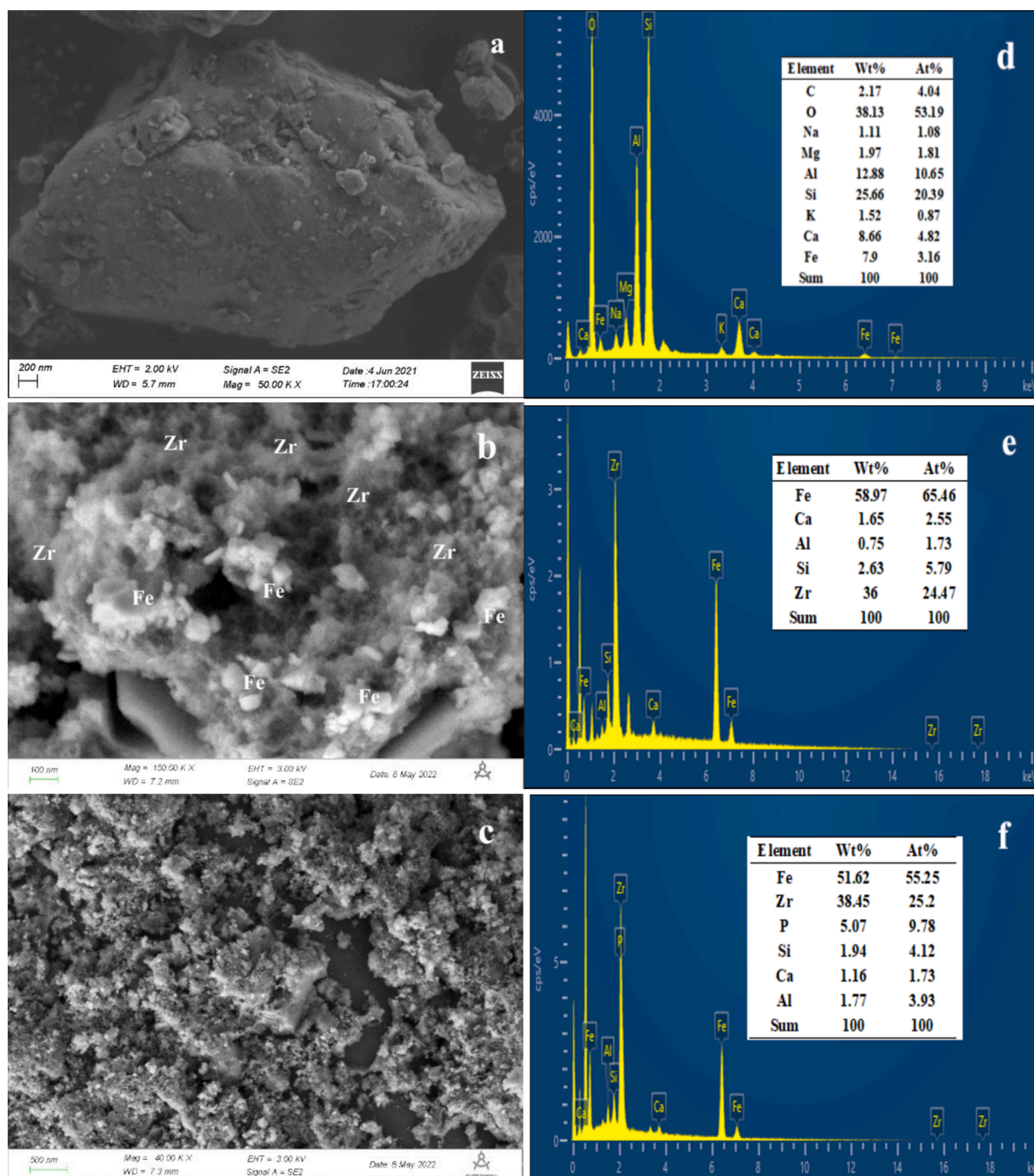


Fig. 8. SEM and EDS spectra of CGCS (a,d), GS-Z2M (b,e) and GS-Z2M after phosphate adsorption (c,f).

mainly involve ligand exchange and inner-sphere complexation.

#### 4. Conclusions

Herein, a series of Zr-doped magnetic gasification CGCS adsorption materials were prepared using a simple one-step co-precipitation method. The adsorbent with a 2:1 ratio of Zr to magnetite (GS-Z2M) showed the best adsorption capacity among the prepared adsorbents, which was attributed to the good adsorption affinity of Zr for phosphate. GS-Z2M was a mesoporous material with a specific surface area of 188 m<sup>2</sup>/g, which is nearly 19 times that of CGCS. It showed the maximum phosphate adsorption capacity of 26.02 mg/g. GS-Z2M almost completely adsorbed phosphate with an initial concentration of 10 mg/L

within 3 h. This adsorption behavior was well described by the Langmuir isotherm and pseudo-second-order models. Notably, GS-Z2M exhibited good phosphate adsorption selectivity. This adsorbent performed well for at least 5 adsorption-desorption cycles, with the phosphate adsorption capacity in the fifth cycle exceeding 57 % of that in the first cycle. Ligand exchange and inner-sphere complexation between GS-Z2M and phosphate were found to be the main adsorption mechanisms. This article proposes a novel phosphate adsorbent prepared by recycling CGCS. Under dynamic flow conditions, GS-Z2M can continuously treat over 199 BV of actual wastewater and 294 BV of synthetic wastewater. This study examined phosphate adsorption in simulated wastewater, followed by adsorption studies on various types of actual wastewater samples. The spent GS-Z2M is expected to be repurposed for use in

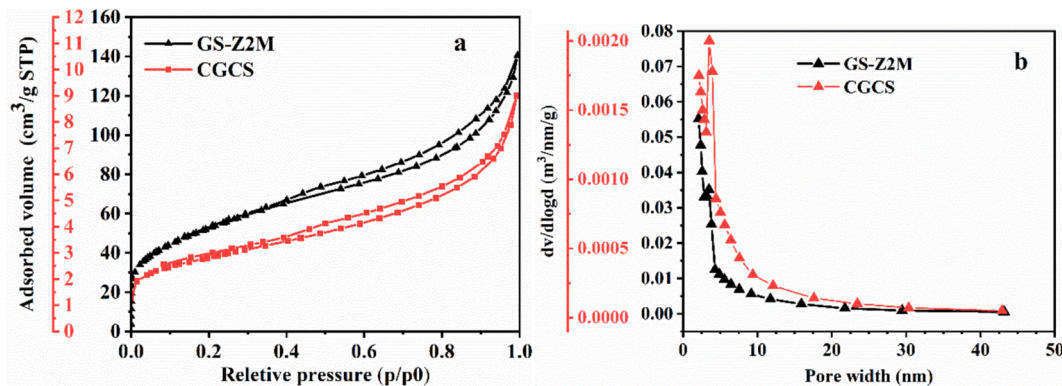


Fig. 9. (a) Nitrogen adsorption–desorption isotherms and (b) pore size distribution of GS-Z2M and CGCS.

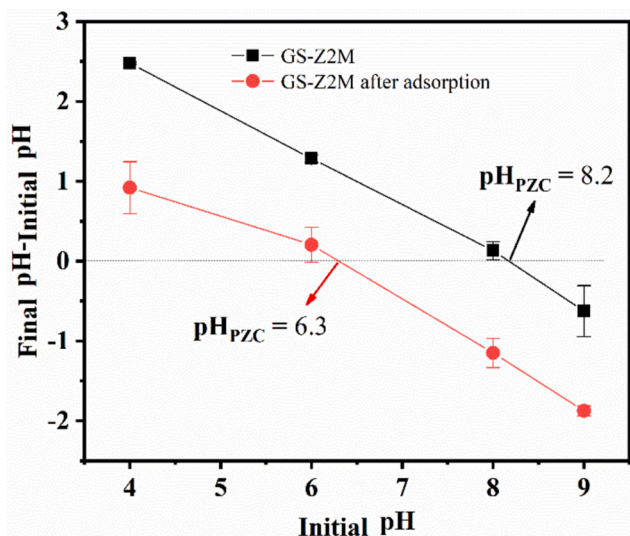


Fig. 10. The  $\text{pH}_{\text{PZC}}$  of GS-Z2M.

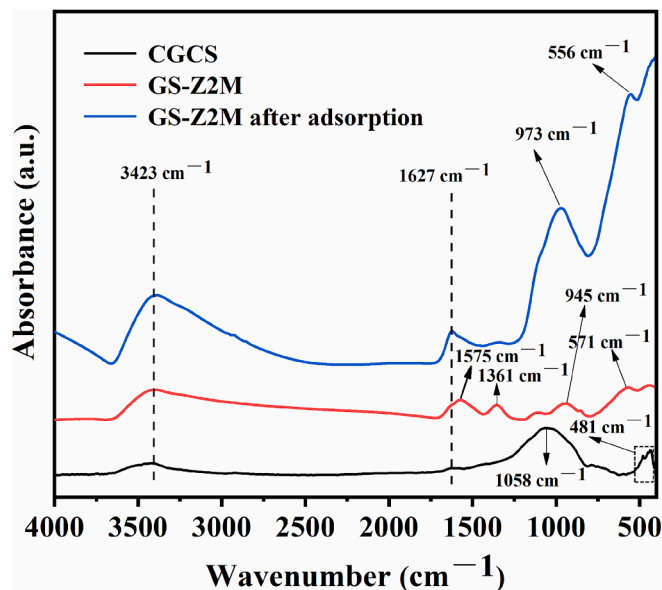


Fig. 12. FTIR spectra of samples.

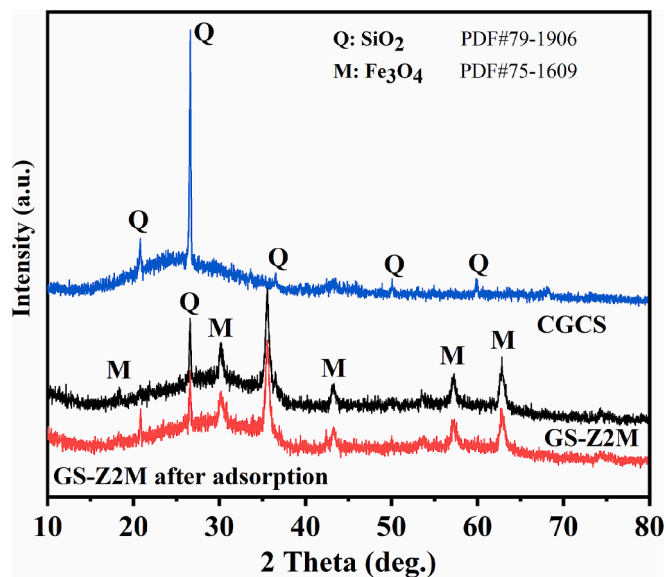


Fig. 11. XRD patterns of CGCS, GS-Z2M and GS-Z2M after adsorption.

functional soils for mine-site greening.

#### CRediT authorship contribution statement

**Baoguo Yang:** Writing – original draft, Validation, Methodology, Investigation, Data curation, Conceptualization. **Fengcheng Jiang:** Writing – review & editing, Resources, Methodology. **Yinxin Zhao:** Writing – review & editing, Resources, Project administration. **Hongbin Li:** Software, Investigation, Formal analysis, Data curation. **Sheng-guang Zhang:** Software, Investigation, Formal analysis, Data curation. **Kanghui Liu:** Writing – review & editing.

#### Declaration of competing interest

The authors declare that they have no known competing financial interests or personal relationships that could have appeared to influence the work reported in this paper.

#### Acknowledgements

This work was supported by Open Project of the Institute of Resources and Ecology at Yili Normal University (YLNURE202304); Xinjiang Uygur Autonomous Region "Tianchi Talents" Program - Young Doctoral Program (2024TYCQNB03); Key Research and Development

Program of Henan (24111320400); China Postdoctoral Science Foundation (2023M731170); Doctoral Fund Project of Henan Polytechnic University (39B2022-39); Key Science and Technology Project of Henan Province (222102320102).

## Appendix A. Supplementary data

Supplementary data to this article can be found online at <https://doi.org/10.1016/j.arabjc.2024.106079>.

## References

- Abdellaoui, Y., Abou Oualid, H., Hsini, A., El Ibrahim, B., Laabd, M., El Ouardi, M., Giacomán-Vallejos, G., Gamero-Melo, P., 2021. Synthesis of zirconium-modified merlineite from fly ash for enhanced removal of phosphate in aqueous medium: experimental studies supported by monte carlo/sa simulations. *Chem. Eng. J.* 404, 126600. <https://doi.org/10.1016/j.cej.2020.126600>.
- Alamgholiloo, H., Pesyan, N.N., Mohammadi, R., Rostamnia, S., Shokouhimehr, M., 2021. Synergistic advanced oxidation process for the fast degradation of ciprofloxacin antibiotics using a go/cumof-magnetic ternary nanocomposite. *J. Environ. Chem. Eng.* 9, 105486. <https://doi.org/10.1016/j.jece.2021.105486>.
- Araújo, C.S.T., Almeida, I.L.S., Rezende, H.C., Marconilio, S.M.L.O., Léon, J.J.L., de Matos, T.N., 2018. Elucidation of mechanism involved in adsorption of pb(II) onto lobeira fruit (*Solanum lycocarpum*) using langmuir, freundlich and temkin isotherms. *Microchem. J.* 137, 348–354. <https://doi.org/10.1016/j.microc.2017.11.009>.
- Aryee, A.A., Dovi, E., Shi, X., Han, R., Li, Z., Qu, L., 2021. Zirconium and iminodiacetic acid modified magnetic peanut husk as a novel adsorbent for the sequestration of phosphates from solution: characterization, equilibrium and kinetic study. *Colloids Surf A Physicochem Eng Asp* 615, 126260. <https://doi.org/10.1016/j.colsurfa.2021.126260>.
- Asaoka, S., Kawakami, K., Saito, H., Ichinari, T., Nohara, H., Oikawa, T., 2021. Adsorption of phosphate onto lanthanum-doped coal fly ash—blast furnace cement composite. *J. Hazard. Mater.* 406, 124780. <https://doi.org/10.1016/j.jhazmat.2020.124780>.
- Bacelo, H., Pintor, A.M.A., Santos, S.C.R., Boaventura, R.A.R., Botelho, C.M.S., 2020. Performance and prospects of different adsorbents for phosphorus uptake and recovery from water. *Chem. Eng. J.* 381, 122566. <https://doi.org/10.1016/j.cej.2019.122566>.
- Coulibaly, L.S., Akpo, S.K., Yvon, J., Coulibaly, L., 2016. Fourier transform infra-red (ftir) spectroscopy investigation, dose effect, kinetics and adsorption capacity of phosphate from aqueous solution onto laterite and sandstone. *J. Environ. Manage.* 183, 1032–1040. <https://doi.org/10.1016/j.jenvman.2016.09.061>.
- Da Silva, J.M., Da Silva, C.E.P., Freire, J.M.A., Becker, H., Diógenes, I.C.N., Longhinotti, E., 2022. Industrial steel waste-based adsorbent: an effective phosphate removal from aqueous media. *Mater. Chem. Phys.* 292, 126828. <https://doi.org/10.1016/j.matchemphys.2022.126828>.
- De Filippis, U., Prud'Homme, E., Meille, S., 2021. Sodium hydroxide substitution in slag activating mixes: a potential pathway to more sustainable slag-based binders. *Constr. Build. Mater.* 300, 124183. <https://doi.org/10.1016/j.conbuildmat.2021.124183>.
- Dou, X., Zhang, Y., Wang, H., Wang, T., Wang, Y., 2011. Performance of granular zirconium-iron oxide in the removal of fluoride from drinking water. *Water Res.* 45, 3571–3578. <https://doi.org/10.1016/j.watres.2011.04.002>.
- Guo, F., Guo, Y., Chen, L., Jia, W., Zhu, Y., Li, Y., Wang, H., Yao, X., Zhang, Y., Wu, J., 2023. Multitudinous components recovery, heavy metals evolution and environmental impact of coal gasification slag: a review. *Chemosphere* 338, 139473. <https://doi.org/10.1016/j.chemosphere.2023.139473>.
- Guo, B., Wang, Y., Qiao, X., Shen, X., Guo, J., Xiang, J., Jin, Y., 2021. Experiment and regeneration kinetic model study on CO<sub>2</sub> adsorbent prepared from fly ash. *Chem. Eng. J.* 421, 127865. <https://doi.org/10.1016/j.cej.2020.127865>.
- He, Y., Lin, H., Dong, Y., Wang, L., 2017. Preferable adsorption of phosphate using lanthanum-incorporated porous zeolite: characteristics and mechanism. *Appl. Surf. Sci.* 426, 995–1004. <https://doi.org/10.1016/j.apsusc.2017.07.272>.
- Huang, X., Zhao, H., Hu, X., Liu, F., Wang, L., Zhao, X., Gao, P., Ji, P., 2020. Optimization of preparation technology for modified coal fly ash and its adsorption properties for Cd<sup>2+</sup>. *J. Hazard. Mater.* 392, 122461. <https://doi.org/10.1016/j.jhazmat.2020.122461>.
- Huo, J., Min, X., Wang, Y., 2021. Zirconium-modified natural clays for phosphate removal: effect of clay minerals. *Environ. Res.* 194, 110685. <https://doi.org/10.1016/j.envres.2020.110685>.
- Jung, K., Lee, S.Y., Choi, J., Lee, Y.J., 2019. A facile one-pot hydrothermal synthesis of hydroxyapatite/biochar nanocomposites: adsorption behavior and mechanisms for the removal of copper(II) from aqueous media. *Chem. Eng. J.* 369, 529–541. <https://doi.org/10.1016/j.cej.2019.03.102>.
- Kegl, T., Kosak, A., Lobnik, A., Novak, Z., Kralj, A.K., Ban, I., 2020. Adsorption of rare earth metals from wastewater by nanomaterials: a review. *J. Hazard. Mater.* 386, 121632. <https://doi.org/10.1016/j.jhazmat.2019.121632>.
- Khan, H., Sharma, S., 2019. Next-generation organometallic adsorbents for safe removal of excessive fluoride from aqueous systems. *J. Appl. Polym. Sci.* 136, 46993. <https://doi.org/10.1002/app.46993>.
- Koh, K.Y., Zhang, S., Paul Chen, J., 2020. Hydrothermally synthesized lanthanum carbonate nanorod for adsorption of phosphorus: material synthesis and optimization, and demonstration of excellent performance. *Chem. Eng. J.* 380, 122153. <https://doi.org/10.1016/j.cej.2019.122153>.
- Koniccki, W., Aleksandrak, M., Moszyński, D., Mijowska, E., 2017. Adsorption of anionic azo-dyes from aqueous solutions onto graphene oxide: equilibrium, kinetic and thermodynamic studies. *J. Colloid Interface Sci.* 496, 188–200. <https://doi.org/10.1016/j.jcis.2017.02.031>.
- Kumar, I.A., Naushad, M., Ahamad, T., Viswanathan, N., 2021. Superficial development of lewis zirconium ion cross-linked gelatin/kaolin hybrid composite for nutrients remediation. *J. Mol. Liq.* 324, 114982. <https://doi.org/10.1016/j.molliq.2020.114982>.
- Li, J., Li, B., Huang, H., Zhao, N., Zhang, M., Cao, L., 2020. Investigation into lanthanum-coated biochar obtained from urban dewatered sewage sludge for enhanced phosphate adsorption. *Sci. Total Environ.* 714, 136839. <https://doi.org/10.1016/j.scitotenv.2020.136839>.
- Liao, T., Li, T., Su, X., Yu, X., Song, H., Zhu, Y., Zhang, Y., 2018. La(OH)<sub>3</sub>-modified magnetic pineapple biochar as novel adsorbents for efficient phosphate removal. *Bioresour. Technol.* 263, 207–213. <https://doi.org/10.1016/j.biortech.2018.04.108>.
- Liu, R., Chi, L., Wang, X., Wang, Y., Sui, Y., Xie, T., Arandiyán, H., 2019a. Effective and selective adsorption of phosphate from aqueous solution via trivalent-metals-based amino-mil-101 mofs. *Chem. Eng. J.* 357, 159–168. <https://doi.org/10.1016/j.cej.2018.09.122>.
- Liu, T., Zheng, S., Yang, L., 2019b. Magnetic zirconium-based metal-organic frameworks for selective phosphate adsorption from water. *J. Colloid Interface Sci.* 552, 134–141. <https://doi.org/10.1016/j.jcis.2019.05.022>.
- Miao, Z., Xu, J., Chen, L., Wang, R., Zhang, Y., Wu, J., 2022. Hierarchical porous composites derived from coal gasification fine slag for CO<sub>2</sub> capture: role of slag particles in the composites. *Fuel* 309, 122334. <https://doi.org/10.1016/j.fuel.2021.122334>.
- Min, X., Wu, X., Shao, P., Ren, Z., Ding, L., Luo, X., 2019. Ultra-high capacity of lanthanum-doped uio-66 for phosphate capture: unusual doping of lanthanum by the reduction of coordination number. *Chem. Eng. J.* 358, 321–330. <https://doi.org/10.1016/j.cej.2018.10.043>.
- Mokrzycki, J., Fedyna, M., Marzec, M., Szerement, J., Panek, R., Klimek, A., Bajda, T., Mierzwa-Hersztel, M., 2022. Copper ion-exchanged zeolite x from fly ash as an efficient adsorbent of phosphate ions from aqueous solutions. *J. Environ. Chem. Eng.* 10, 108567. <https://doi.org/10.1016/j.jece.2022.108567>.
- Navarro, C., Díaz, M., Villa-García, M.A., 2010. Physico-chemical characterization of steel slag. Study of its behavior under simulated environmental conditions. *Environ. Sci. Technol.* 44, 5383–5388. <https://doi.org/10.1021/es100690b>.
- Peng, R., Xin, R., Wu, D., Zhu, W., Li, Y., Zhai, S., 2024. Biomass: the accelerator for moving mofs to practical applications. *Chem. Eng. J. (Lausanne, Switzerland: 1996)* 497, 154908. <https://doi.org/10.1016/j.cej.2024.154908>.
- Qiu, B., Duan, F., 2019. Synthesis of industrial solid wastes/biochar composites and their use for adsorption of phosphate: from surface properties to sorption mechanism. *Colloids Surf. A Physicochem. Eng. Asp.* 571, 86–93. <https://doi.org/10.1016/j.colsurfa.2019.03.041>.
- Shan, S., Tang, H., Zhao, Y., Wang, W., Cui, F., 2019. Highly porous zirconium-crosslinked graphene oxide/alginate aerogel beads for enhanced phosphate removal. *Chem. Eng. J.* 359, 779–789. <https://doi.org/10.1016/j.cej.2018.10.033>.
- Shu, Q., Sun, Z., Zhu, G., Wang, C., Li, H., Qi, F., Zhang, Q., Li, S., 2022. Highly efficient synthesis of zsm-5 zeolite by one-step microwave using desiccation solution of coal gasification coarse slag and its application to vocs adsorption. *Process Saf. Environ. Protect.* 167, 173–183. <https://doi.org/10.1016/j.psep.2022.08.068>.
- Su, S., Tahir, M.H., Cheng, X., Zhang, J., 2024. Modification and resource utilization of coal gasification slag-based material: a review. *J. Environ. Chem. Eng.* 12, 112112. <https://doi.org/10.1016/j.jece.2024.112112>.
- Sun, J., Xiu, Y., Huang, K., Yu, J., Alam, S., Zhu, H., Guo, Z., 2018. Selective recovery of phosphorus from acid leach liquor of iron ore by garlic peel adsorbent. *Rsc Adv.* 8, 22276–22285. <https://doi.org/10.1039/c8ra03203c>.
- Thommes, M., Kaneko, K., Neimark, A.V., Olivier, J.P., Rodriguez-Reinos, F., Rouquerol, J., Sing, K.S.W., 2015. Physisorption of gases, with special reference to the evaluation of surface area and pore size distribution (iupac technical report). *Pure Appl. Chem.* 87, 1051–1069. <https://doi.org/10.1515/pac-2014-1117>.
- Usman, M.A., Khan, A.Y., 2022. Selective adsorption of anionic dye from wastewater using polyethyleneimine based macroporous sponge: batch and continuous studies. *J. Hazard. Mater.* 428, 128238. <https://doi.org/10.1016/j.jhazmat.2022.128238>.
- Varas, M.J., Alvarez De Buergo, M., Fort, R., 2005. Natural cement as the precursor of portland cement: methodology for its identification. *Cem. Concr. Res.* 35, 2055–2065. <https://doi.org/10.1016/j.cemconres.2004.10.045>.
- Wang, H., Fu, Y., Wang, X., Gao, J., Zhang, Y., Zhao, Q., 2015. Preparation and performance of tubular nanoflaky (ni, co, mn) oxides with hierarchical mesoporous structure. *J. Alloy. Compd.* 639, 352–358. <https://doi.org/10.1016/j.jallcom.2015.03.178>.
- Wu, Y., Xue, K., Ma, Q., Ma, T., Ma, Y., Sun, Y., Ji, W., 2021. Removal of hazardous crystal violet dye by low-cost p-type zeolite/carbon composite obtained from in situ conversion of coal gasification fine slag. *Micropor. Mesopor. Mat.* 312, 110742. <https://doi.org/10.1016/j.micromeso.2020.110742>.
- Xie, Q., Lin, Y., Wu, D., Kong, H., 2017. Performance of surfactant modified zeolite/hydrous zirconium oxide as a multi-functional adsorbent. *Fuel* 203, 411–418. <https://doi.org/10.1016/j.fuel.2017.04.141>.
- Xiong, W., Tong, J., Yang, Z., Zeng, G., Zhou, Y., Wang, D., Song, P., Xu, R., Zhang, C., Cheng, M., 2017. Adsorption of phosphate from aqueous solution using iron-zirconium modified activated carbon nanofiber: performance and mechanism. *J. Colloid Interface Sci.* 493, 17–23. <https://doi.org/10.1016/j.jcis.2017.01.024>.
- Xu, C., Xu, Y., Zhong, D., Chang, H., Mou, J., Wang, H., Shen, H., 2022. Efficient adsorption and reduction of cr(vi) by Zr<sup>2+</sup> cross-linked magnetic chitosan/

- polyaniline composite. *J. Environ. Chem. Eng.* 10, 108977. <https://doi.org/10.1016/j.jece.2022.108977>.
- Yang, Y., Wang, Y., Zheng, C., Lin, H., Xu, R., Zhu, H., Bao, L., Xu, X., 2022. Lanthanum carbonate grafted zsm-5 for superior phosphate uptake: investigation of the growth and adsorption mechanism. *Chem. Eng. J. (Lausanne, Switzerland: 1996)* 430, 133166. [10.1016/j.cej.2021.133166](https://doi.org/10.1016/j.cej.2021.133166).
- Yang, B., Han, F., Xie, Z., Yang, Z., Jiang, F., Yang, S., Li, Y., 2022a. Study on adsorption of phosphate from aqueous solution by zirconium modified coal gasification coarse slag. *Rsc Adv.* 12, 17147–17157. <https://doi.org/10.1039/d2ra02263j>.
- Yang, B., Han, F., Bai, Y., Xie, Z., Shi, T., Wang, J., Li, Y., 2023a. Phosphate removal performance and mechanism of magnesium–lanthanum–modified coal gasification coarse slag. *Mater. Today Sustain.* 22, 100357. <https://doi.org/10.1016/j.mtsust.2023.100357>.
- Yang, B., Han, F., Li, Y., Bai, Y., Xie, Z., Yang, J., Liu, T., 2023b. Phosphate removal mechanism of a novel magnesium slag-modified coal gasification coarse slag adsorbent. *Environ. Sci. Pollut. Res. Int.* 30, 60607–60617. <https://doi.org/10.1007/s11356-023-26667-1>.
- Yang, H., Li, S., Shan, X., Yang, C., An, Q., Zhai, S., Xiao, Z., 2021. Hollow polyethyleneimine/carboxymethyl cellulose beads with abundant and accessible sorption sites for ultra-efficient chromium (VI) and phosphate removal. *Sep. Purif. Technol.* 278, 119607. <https://doi.org/10.1016/j.seppur.2021.119607>.
- Yang, B., Li, Y., Han, F., Bai, Y., Zhang, Y., Yu, J., Fu, Z., 2023c. Novel composite in situ obtained from coal gasification coarse slag and its mechanism of removing phosphate. *Arab. J. Chem.* 16, 104512. <https://doi.org/10.1016/j.arabjc.2022.104512>.
- Yang, Y., Liu, D., Chen, Y., He, J., Li, Q., 2024a. Mechanistic study of highly effective phosphate removal from aqueous solutions over a new lanthanum carbonate fabricated carbon nanotube film. *J. Environ. Manage.* 359, 120938. <https://doi.org/10.1016/j.jenvman.2024.120938>.
- Yang, Y., Liu, M., Tang, S., You, X., Li, Y., Mei, Y., Chen, Y., 2024b. Investigation of the key mechanisms and optimum conditions of high-effective phosphate removal by bimetallic la-fe-cnt film. *Sep. Purif. Technol.* 341, 126938. <https://doi.org/10.1016/j.seppur.2024.126938>.
- Yang, L., Shan, X., Zhao, Y., Xiao, Z., An, Q., Zhai, S., 2022b. Efficient phosphate capture of Fe<sub>3</sub>O<sub>4</sub>/UIO-66-NH<sub>2</sub>/CeO<sub>2</sub> in wide pH spectrum. *Micropor. Mesopor. Mat.* 331, 111653. <https://doi.org/10.1016/j.micromeso.2021.111653>.
- Yang, Y., Yuen Koh, K., Li, R., Zhang, H., Yan, Y., Chen, J.P., 2020. An innovative lanthanum carbonate grafted microfibrillar composite for phosphate adsorption in wastewater. *J. Hazard. Mater.* 392, 121952. <https://doi.org/10.1016/j.jhazmat.2019.121952>.
- Yin, H., Kong, M., Gu, X., Chen, H., 2017. Removal of arsenic from water by porous charred granulated attapulgite-supported hydrated iron oxide in bath and column modes. *J. Clean Prod.* 166, 88–97. <https://doi.org/10.1016/j.jclepro.2017.08.026>.
- Yu, Y., Yu, L., Paul Chen, J., 2015. Adsorption of fluoride by Fe–Mg–La triple-metal composite: adsorbent preparation, illustration of performance and study of mechanisms. *Chem. Eng. J.* 262, 839–846. <https://doi.org/10.1016/j.cej.2014.09.006>.
- Yuan, N., Tan, K., Zhang, X., Zhao, A., Guo, R., 2022. Synthesis and adsorption performance of ultra-low silica-to-alumina ratio and hierarchical porous ZSM-5 zeolites prepared from coal gasification fine slag. *Chemosphere* 303, 134839. <https://doi.org/10.1016/j.chemosphere.2022.134839>.
- Zhao, R., Ma, T., Zhao, S., Rong, H., Tian, Y., Zhu, G., 2020. Uniform and stable immobilization of metal-organic frameworks into chitosan matrix for enhanced tetracycline removal from water. *Chem. Eng. J.* 382, 122893. <https://doi.org/10.1016/j.cej.2019.122893>.
- Zhou, J., Yang, S., Yu, J., Shu, Z., 2011. Novel hollow microspheres of hierarchical zinc–aluminum layered double hydroxides and their enhanced adsorption capacity for phosphate in water. *J. Hazard. Mater.* 192, 1114–1121. <https://doi.org/10.1016/j.jhazmat.2011.06.013>.
- Zhu, Y., Wu, J., Zhang, Y., Miao, Z., Niu, Y., Guo, F., Xi, Y., 2024. Preparation of hierarchically porous carbon ash composite material from fine slag of coal gasification and ash slag of biomass combustion for CO<sub>2</sub> capture. *Sep. Purif. Technol.* 330, 125452. <https://doi.org/10.1016/j.seppur.2023.125452>.
- Zhu, D., Yang, H., Chen, X., Chen, W., Cai, N., Chen, Y., Zhang, S., Chen, H., 2021. Temperature-dependent magnesium citrate modified formation of mgo nanoparticles biochar composites with efficient phosphate removal. *Chemosphere* 274, 129904. <https://doi.org/10.1016/j.chemosphere.2021.129904>.